Journal of Dynamics, Monitoring and Diagnostics, 2022, 1, 208-222
https://doi.org/10.37965/jdmd.2022.108

RESEARCH ARTICLE

Dynamic Response Analysis of A 5 MW NREL Wind Turbine Blade under Flap-Wise and Edge-Wise Vibrations

Amna Algolfat,[1] Weizhuo Wang,[1] and Alhussein Albarbar[1]
[1]Infrastructure and Industry Research Group, Department of Engineering,
Manchester Metropolitan University, Manchester, M1 5GD, UK

(Received 12 April 2022; Revised 08 June 2022; Accepted 12 July 2022; Published online 13 September 2022)

Abstract: A wind turbine is subjected to a regime of varying loads. For example, each rotor revolution causes a complete gravity stress reversal in the low-speed shaft, and there are varying stresses from the out-of-plane loading cycle due to fluctuating wind load. Consequently, wind turbine blade design is governed by fatigue rather than ultimate load considerations. Previous studies have adopted many different beam theories, using different techniques and codes, to model the National Renewable Energy Laboratory (NREL) 5 MW offshore wind turbine blade. There are differences, from study to study, in the free vibration results and the dynamic response. The contribution of this study is to apply the code written by the authors to the different beam theories used with the aim of comparing the different beam theories presented in the literature and that developed by the authors. This paper reports the investigation of the effects of deformation parameters on the dynamic characteristics of the NREL 5 MW offshore wind turbine blades predicted by the different beam theories. The investigation of free vibrations is a fundamental step in the analysis of structural dynamics, and this study compares different computational structural methods and investigates their effect on the predicted dynamic response. The modal characteristics of every model examined have been combined with strip theory to determine the dynamic response of the blade.

Key words: blade dynamic response; edge-wise vibration; free vibration analysis; flap-wise vibration; wind turbine vibration

Nomenclature:

L	Blade length (m)
D	Rotor diameter (m)
E	Modulus of elasticity (N/m^2)
A	Blade cross-sectional area (m^2)
I	Blade moment of inertia (m^4)
$\boldsymbol{K}$	Kinetic energy (J)
U	Potential energy (J)
$\mathcal{W}$	Work due to external distributed force (J)
$\boldsymbol{w}$	Flap-wise displacement (m)
$\boldsymbol{f}$	External force (N)
t	Time (s)
R	Hub radius (m)
g	Gravitational acceleration (m/s^2)
$\boldsymbol{T}$	Axial force due to centrifugal tension (N)
$\boldsymbol{u}$	Flap-wise deflection (m)
$\boldsymbol{v}$	Edge-wise deflection (m)
$\boldsymbol{x}$	Distance relative to the blade span (m)
$\boldsymbol{\rho}$	The blade density (kg/m^3)
$\boldsymbol{\Omega}$	Angular velocity of the blade (r/min)
$\boldsymbol{\varkappa}$	Timoshenko's shear coefficient
$\boldsymbol{\theta_p}$	Pitch angle (deg)
$\boldsymbol{\theta_T}$	Twist angle (deg)
ϑ	Precone angle (deg)
$\boldsymbol{\alpha}$	Angle of attack (deg)
$\boldsymbol{\beta}$	Total pitch angle (deg)
$\boldsymbol{\theta}$	Azimuth position of the blade
$\boldsymbol{\omega}$	Natural frequency(rad/s)
X$_h$	Hub X-axis
Y$_h$	Hub Y-axis
G	Local gyroscopic matrix
m	Local mass matrix
k	Local stiffness matrix
$\mathfrak{f}_N$	Normal aerodynamic force (N)
$\mathfrak{f}_T$	Tangential aerodynamic force (N)
$\boldsymbol{\beta}$	Total pitch angle (rad)
$\boldsymbol{a},\boldsymbol{a}'$	The induction velocity factors
$\mathcal{L}$	Lift force
$\mathcal{D}$	Drag force
$\boldsymbol{\rho_a}$	Airflow density
$\boldsymbol{C_l}$	The lift coefficient
$\boldsymbol{C_d}$	Drag coefficient
$\boldsymbol{U_a}$	Airflow velocity (m/s)
$\boldsymbol{F_{ext}}$	Column matrix of the excitation forces and/or moments
$\boldsymbol{c}$	Chord length (m)
OHAWT	Offshore horizontal axis wind turbine
NREL	National Renewable Energy Laboratory
BEM	Blade element momentum
TB	Timoshenko beam

I. INTRODUCTION

The global statistics of investment rate in wind energy indicate the rapidly increasing importance of this energy source worldwide [1]. However, wind turbines as a reliable source of green energy require further improvement to ensure the reliability of offshore wind turbines. Professor Heronemus first proposed the application of offshore wind turbines as a source of wind energy [2]. However, even countries such as the UK with its long shoreline and many offshore wind turbines produce only 13% of total UK

Corresponding author: Amna Algolfat (e-mail: Amnaalgolfat@hotmail.com).

electricity generated today [3]; thus, questions remain as to whether offshore sources can provide a sufficiently large growth in wind energy across the world in time to meet demand.

The blade is considered one of the most critical components in a wind turbine, being a major contributor to downtime and accounting for over 41% of total failures [4]. The challenge to produce the required energy is further complicated as the size of the blade becomes larger, and wind turbines are positioned in more challenging terrain [5,6]. Calculating the dynamic response of the wind turbine blade requires investigation of the free vibration to determine the modal characteristics [7]. The structural analysis of composite blades is frequently performed as a three-dimensional (3D) finite element model using solid or shell elements in commercial software such as ANSYS and ABAQUS [8,9], while [10,11] used a multibody dynamic model in structural analysis of the blade.

The blade may be discretized into several rigid or flexible bodies with revolutes joint connecting them. The FAST code [12] developed by the National Renewable Energy Laboratory (NREL) to simulate the dynamic response of a horizontal axis wind turbine (HAWT) uses the lumped mass technique to model the structure of the blade [12]. The Bonus Horizontal Axis Wind Turbine Code that Siemens Wind Power developed uses finite elements to model the wind turbine blade as Timoshenko beam elements [13].

Free vibration analysis is a fundamental step in the analysis of structural dynamics. Different codes [7] have adopted different techniques to analyze the free vibration of the blade according to the structural details that need to be addressed. The composite wind turbine blade can be modeled by a beam. Timoshenko beam theory is used in [14] to analyze the blade structure. The work in [15] uses Rayleigh beam theory and incorporates the influence of the pitch and precone angles on the dynamic characteristics of the HAWT blade in the flap-wise direction to carry out free vibration analysis to determine the blade's modal characteristics.

The study in [16] adopted the geometrically exact beam theory to find the natural frequencies and corresponding mode shapes in the flap-wise and edge-wise directions to find the deflection response in both directions. The influence of different blade parameters on the flap-wise vibrations was studied in [17], where the effects of such parameters on dynamic characteristics of NREL 5 MW wind turbine blades were investigated using different beam theories. In [17], the mode shape comparisons were carried out using modal scale factor and modal assurance criteria to study the correlation between the different theories used. The study found that Bernoulli's algorithms produce less accurate results than Rayleigh and Timoshenko beam theories. The Euler–Bernoulli beam theory is considered in [18] for structural modeling. The modal properties of the blade were obtained in [18] using the ANSYS commercial finite element software, but it did not consider gyroscopic effects due to the low nominal rotational speed of the blade. In the same study, the aerodynamic loading was calculated using the 3D aerodynamics of the rotating blade based on the blade momentum theory. The work in [19] investigated the influence of centrifugal stiffening on the free vibrations and dynamic response of offshore wind turbine blades. The study adopted the Rayleigh beam theory to analyze the blade structure. A significant advance was made in [15] by scrutinizing the effects of harmonic excitation due to the gravitational force, precone, and pitch angles, based on Rayleigh beam theory. However, the study did not apply the different methods to a blade with the same geometry. Furthermore, despite mentioning the significance of pitch and precone angles with increasing rotational speed, the results did not quantify their effect on the dynamic response of the blade. A refined mesh is required for 3D Finite Element Method (FEM) because the complicated characteristics of composite blades need increased computational time [8,9]. The continuity of adjacent sections is poor in the multibody dynamic model, despite having a higher computation efficiency [10,11].

Several techniques are used to calculate the aerodynamic loading based on the above combinations of structural analysis of wind turbine blades. Blade element momentum (BEM) theory was used in [16], and the same BEM theory was employed to calculate the aerodynamic forces [18–21]. The computational fluid dynamics (CFD) technique was adopted in [10,22,23]. Most researchers use approaches based on the blade element momentum theory by integrating the two-dimensional aerofoil aerodynamic loading along the blade's different sections. In this study, due to the short computational time and satisfactory results, BEM is chosen to calculate the normal and tangential forces.

It is not straightforward to include all structural details of composite blades in vibration analysis. Different beam theories are incorporated in [4,14,15,15,16,24]. Each theory has its structural details and considers different stress deformations. The work in [17] found that Bernoulli's algorithms produce less accurate free vibration results than Rayleigh and Timoshenko beam theories. This study is based on structural modeling that adopted [17] for free vibration analysis and used the results to find the difference in dynamic deflection between the adopted theories. This study employs various beam theories to analyze the structural dynamics of the blade. The aim is to compare different beam theories on free vibration and find the effect of the predicted different free vibration data on the dynamic response. A finite element code has been written using the specification of the 5 MW NREL blade for structural modeling and simulation studies. The contribution of this study is to apply the same code using the same numerical techniques to all relevant beam theories. The aim is to make a comparison between the predictions made in this study and those found in the literature for the different beam theories. The study incorporates the effects of different deformation parameters and pursues their influences on the dynamic characteristics by using different beam theories. Then, the dynamic response is calculated as the sum of the products of forces based on each theory and the discrepancies in net energy of each theory observed. The modal characteristics of all the models examined are combined with the strip theory and used to determine the dynamic response of the blade.

II. MODELING

The specification of a 5 MW NREL offshore blade, as shown in Fig. 1, is used for modeling and validation [12]. This study investigates the different stress parameters on the dynamic response and builds an accurate dynamic prediction model of offshore wind turbine blades. In this section, the computational structural model will be presented. Then the model parameters will be extracted. The aerodynamic loading and dynamic response models will be developed to

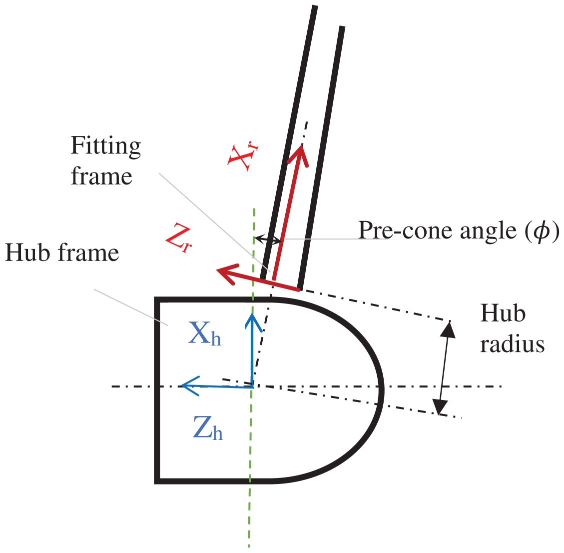

Fig. 1. Blade root coordinate frames of 5 MW wind turbine blade.

portray the comprehensive model of the offshore HAWT blade under the flap-wise and edge-wise vibrations. The blade is dominantly deformed due to the different and complex aerodynamic loads. Thus, the study considers the different stress deformations in order to extract the model parameters, such as the stiffness, frequencies, mode shapes, and forced response. All these parameters will be affected by the stress deformation state of the blade.

A. STRUCTURAL MODELING

In this study, a nonlinear beam model based on different beam theories is employed to determine the effect of including different stress deformations on the model parameters. The blade is considered to rotate at an angular velocity Ω. The blade undergoes flexural bending vibration in the flap-wise and edge-wise directions, and the governing equation can be obtained by using the variational principle. For a HAWT blade, the Lagrangian function is given by [17]:

$$L = K - U + \mathcal{W} \tag{1}$$

The total kinetic energy of the HAWT blade due to the flap-wise vibration is

$$K = K_1 + K_2 + K_3 \tag{2}$$

The first term is due to the flexural bending and can be expressed as [17]:

$$K_1 = \frac{1}{2}\int_0^L \rho A(x)\left(\frac{\partial w(x,t)}{\partial t}\right)^2 \mathrm{d}x \tag{3}$$

The second term is for the kinetic energy resulting from the rotary inertia of the blade, and it can be expressed as:

$$K_2 = \frac{1}{2}\int_0^L \left[\rho I_{zz}^*(x)\left(\frac{\partial^2 w(x,t)}{\partial x \partial t}\right)^2 + \rho I_{zz}^*(x)\Omega^2\left(\frac{\partial w(x,t)}{\partial x}\right)^2\right]\mathrm{d}x \tag{4}$$

where $I^* = I(x)cos^2(\vartheta)$, and ϑ is the precone angle.

The last term in the expression for the kinetic energy is the result of adding the effects of precone and pitch angles and comes from the fact that the axis of rotation is not parallel with the flap-wise direction of the blade [15]:

$$\begin{aligned} K_3 = \frac{1}{2}\int_0^L \Big[& -\frac{1}{8}\rho(x)A(x)\Omega^2(2\cos(2\vartheta) \\ & + \cos(2(\vartheta - \theta_p)) + 2\cos(2\theta_p) \\ & + \cos(2(\vartheta + \theta_p)) - 6)w(x,t)^2\Big]\mathrm{d}x \end{aligned} \tag{5}$$

where $\rho(x)$ represents the blade density, $A(x)$ represents blade cross-sectional area in the flap-wise direction at distance x relative to the blade span, $I(x)$ represents blade moment of inertia, L is the blade length, Ω is the angular velocity of the blade, ϑ is the precone angle, θ_p is the pitch angle, and $w(x,t)$ is the flap-wise bending displacement. The potential energy of the HAWT blade is

$$U = U_1 + U_2 \tag{6}$$

The strain energy of the blade due to flexural bending is [17]

$$U_1 = \frac{1}{2}\int_0^L EI^*(x)\left(\frac{\partial^2 w}{\partial x^2}\right)^2 \mathrm{d}x \tag{7}$$

where $EI^* = EI(x)\cos^2(\vartheta)$.

The potential energy due to the centrifugal and gravitational forces is [17,25]

$$U_2 = \frac{1}{2}\int_0^l T(x,t)\left(\frac{\partial w}{\partial x}\right)^2 \mathrm{d}x \tag{8}$$

and $T(x,t) = T_c(x) + T_g(x,t)$

$$\begin{aligned} T(x,t) = \frac{1}{2}\int_x^l & [(\rho(x)A(x)\Omega^2(R + x\cos(\vartheta)) \\ & - \rho(x)A(x)g\,\cos(\theta)\cos(\vartheta)]\mathrm{d}x \end{aligned} \tag{9}$$

where $T(x,t)$ is the axial tension due to the centrifugal force $T_c(x)$ and the gravitational force component $T_g(x,t)$ at a distance x from the center of rotation, as shown in Fig. 2.

Hamilton's principle can be stated as:

$$\delta\int_{t1}^{t2}(K - U + \mathcal{W})\mathrm{d}t = 0 \tag{10}$$

Since $\delta w = 0 \; at \; t = t_1$ and $t = t_2$, it follows that the governing equation of motion for the Rayleigh theory in the flap-wise (out-of-plane) direction includes the control angle effect and can be obtained as:

$$\begin{aligned} & \rho A(x)\frac{\partial^2 w}{\partial t^2} + \frac{\partial^2}{\partial x^2}\left(EI_{zz}^*(x)\frac{\partial^2 w}{\partial x^2}\right) - \frac{\partial}{\partial x}\left(T(x,t)\frac{\partial w}{\partial x}\right) \\ & \quad - \frac{\partial}{\partial x}\left(\rho I_{zz}^*(x)\frac{\partial^3 w}{\partial x \partial t^2}\right) + \Omega^2\frac{\partial}{\partial x}\left(\rho I_{zz}^*(x)\frac{\partial w}{\partial x}\right) - k(x)w \\ & = f(x,t) \end{aligned} \tag{11}$$

In the same manner, the forced edge-wise (in-plane) direction of the nonuniform beam is obtained as:

$$\begin{aligned} & \rho A(x)\frac{\partial^2 v}{\partial t^2} + \frac{\partial^2}{\partial x^2}\left(EI_{yy}^*(x)\frac{\partial^2 v}{\partial x^2}\right) - \frac{\partial}{\partial x}\left(T(x,t)\frac{\partial v}{\partial x}\right) \\ & \quad - \frac{\partial}{\partial x}\left(\rho I_{yy}^*(x)\frac{\partial^3 v}{\partial x \partial t^2}\right) + \Omega^2\frac{\partial}{\partial x}\left(\rho I_{yy}^*(x)\frac{\partial v}{\partial x}\right) - k(x)v \\ & = f(x,t) \end{aligned} \tag{12}$$

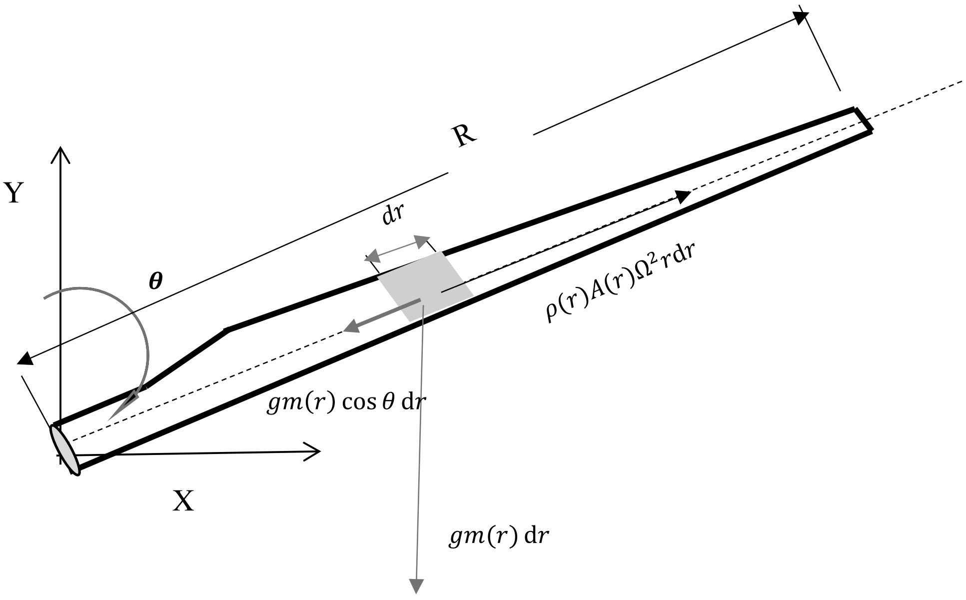

Fig. 2. The restoring force due to centrifugal and axial component of gravitational forces.

Applying numerical methods, the blade model is discretized into a number of elements. According to each beam theory, the governing equation of each beam element is linearized as [25]:

$$[\boldsymbol{M}]\{\ddot{q}\}+[\boldsymbol{C}]\{\dot{q}\}+[\boldsymbol{K}]\{q\}=\{F_{ext}-F\} \tag{13}$$

where M, C, and K are, respectively, the local matrices for the mass, damping, and stiffness of the blade element. $\ddot{q}$, $\dot{q}$, and q are the generalized acceleration, velocity, and displacement, respectively, while F_{ext} is the sum of local applied forces, including aerodynamic and gravitational forces and F is the sum of the relevant components of the elemental forces.

B. APPLICABILITY OF EULER–BERNOULLI, RAYLEIGH, AND TIMOSHENKO BEAM THEORIES TO FLAP-WISE AND EDGE-WISE DEFORMATION

If only the first two terms of Eq. (11) are considered, the Euler–Bernoulli beam's governing equation for the forced flap-wise vibration of nonuniform and nonrotating beams in the flap-wise direction is obtained as:

$$\rho A(x)\frac{\partial^2 w(x,t)}{\partial t^2}+\frac{\partial^2}{\partial x^2}\left(EI^*_{zz}(x)\frac{\partial^2 w(x,t)}{\partial x^2}\right)=f(x,t) \tag{14}$$

The Euler–Bernoulli beam's governing equation for the forced edge-wise vibration of nonuniform and nonrotating beams in the edge-wise direction is then obtained as:

$$\rho A(x)\frac{\partial^2 v(x,t)}{\partial t^2}+\frac{\partial^2}{\partial x^2}\left(EI^*_{yy}(x)\frac{\partial^2 v(x,t)}{\partial x^2}\right)=f(x,t) \tag{15}$$

If the third term of Eq. (11) is added, the Euler–Bernoulli rotating beam's governing equation for the forced flap-wise vibration of a nonuniform beam is obtained as:

$$\rho A(x)\frac{\partial^2 w(x,t)}{\partial t^2}+\frac{\partial^2}{\partial x^2}\left(EI^*_{zz}(x)\frac{\partial^2 w(x,t)}{\partial x^2}\right)-\frac{\partial}{\partial x}\left(T(x,t)\frac{\partial w(x,t)}{\partial x}\right)=f(x,t) \tag{16}$$

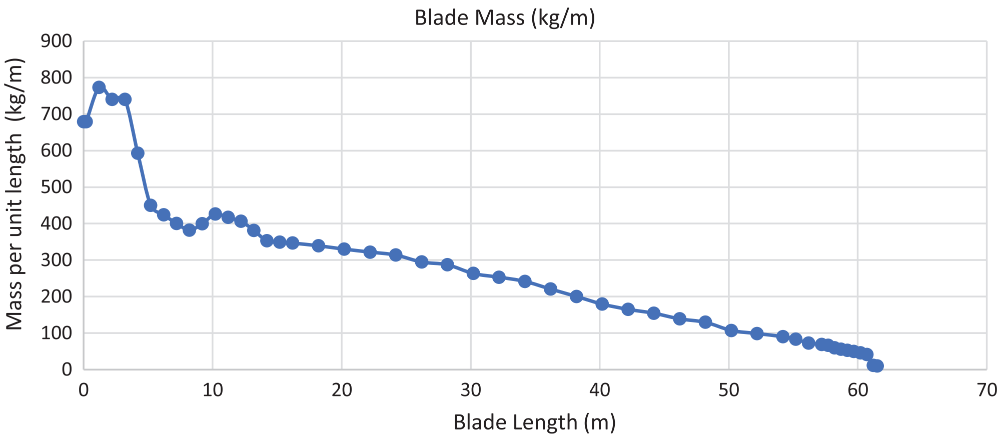

Fig. 3. The mass per unit length (ρA) distribution spanwise along the NREL 5 MW blade [12].

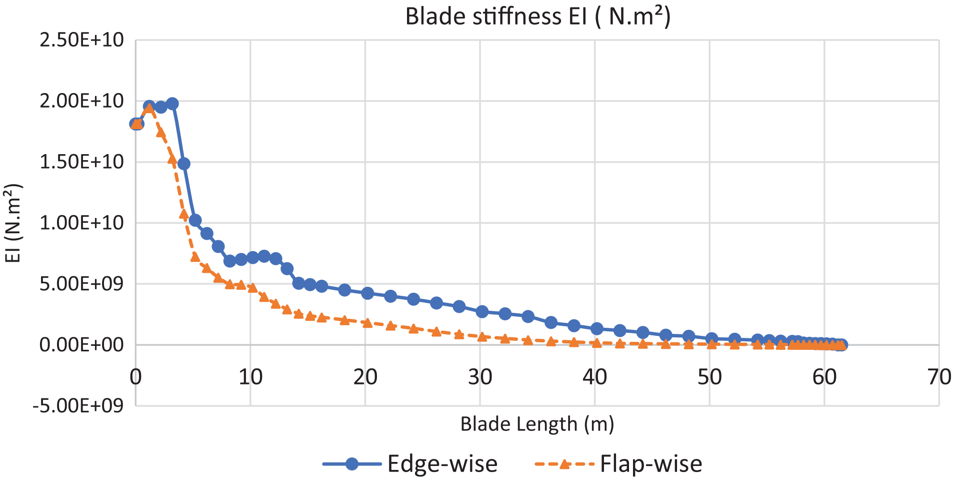

Fig. 4. The flap-wise and edge-wise flexural rigidity (EI) distribution along the NREL 5 MW blade span [12].

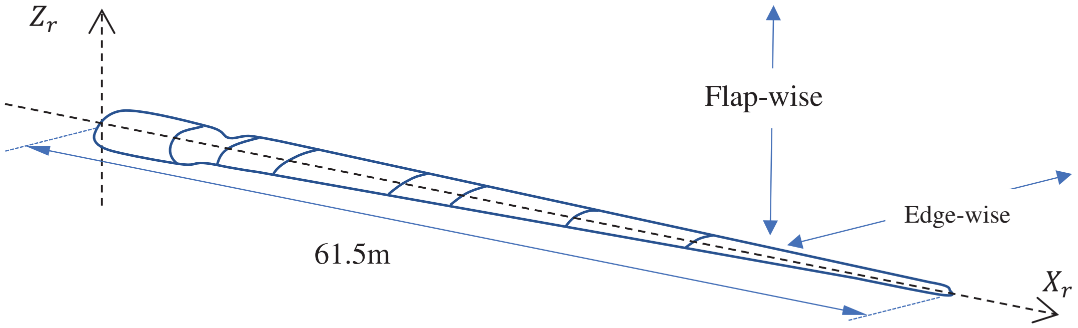

Fig. 5. Deformation directions of 5 MW NREL blade.

and the Euler–Bernoulli rotating beam's governing equation for the forced edge-wise vibration of nonuniform beam is obtained as:

$$\rho A(x)\frac{\partial^2 v(x,t)}{\partial t^2}+\frac{\partial^2}{\partial x^2}\left(EI^*_{yy}(x)\frac{\partial^2 v(x,t)}{\partial x^2}\right)-\frac{\partial}{\partial x}\left(T(x,t)\frac{\partial v(x,t)}{\partial x}\right)=f(x,t) \tag{17}$$

where $f(x,t)$ is the external distributed load along the beam span.

The governing equation for a rotating Rayleigh beam in the flap-wise direction can be expressed directly from Eq. (11) by neglecting the terms containing the effect of precone and pitch angles to be as:

$$\rho A(x)\frac{\partial^2 w}{\partial t^2}+\frac{\partial^2}{\partial x^2}\left(EI^*_{zz}(x)\frac{\partial^2 w}{\partial x^2}\right)-\frac{\partial}{\partial x}\left(T(x,t)\frac{\partial w}{\partial x}\right)-\frac{\partial}{\partial x}\left(\rho I^*_{zz}(x)\frac{\partial^3 w}{\partial x\partial t^2}\right)+\Omega^2\frac{\partial}{\partial x}\left(\rho I^*_{zz}(x)\frac{\partial w}{\partial x}\right)=f(x,t) \tag{18}$$

For the edge-wise vibration, we have

$$\rho A(x)\frac{\partial^2 w}{\partial t^2}+\frac{\partial^2}{\partial x^2}\left(EI^*_{yy}(x)\frac{\partial^2 w}{\partial x^2}\right)-\frac{\partial}{\partial x}\left(T(x,t)\frac{\partial w}{\partial x}\right)-\frac{\partial}{\partial x}\left(\rho I^*_{yy}(x)\frac{\partial^3 w}{\partial x\partial t^2}\right)+\Omega^2\frac{\partial}{\partial x}\left(\rho I^*_{yy}(x)\frac{\partial w}{\partial x}\right)=f(x,t) \tag{19}$$

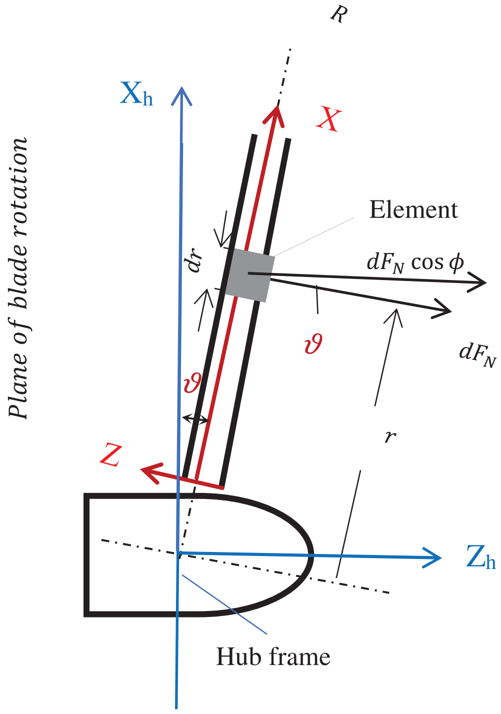

Fig. 6. Aerodynamic normal force at a blade element.

Timoshenko beam theory, for the forced flap-wise vibration of a nonuniform beam, is obtained as [26]:

$$\frac{\partial^2}{\partial x^2}\left(EI^*_{zz}(x)\frac{\partial^2 w(x,t)}{\partial x^2}\right)+\rho A(x)\frac{\partial^2 w(x,t)}{\partial t^2} -\frac{\partial}{\partial x}\left(\rho I^*_{zz}(x)\left(1+\frac{E}{\varkappa G}\right)\frac{\partial^3 w}{\partial x\partial t^2}\right) +\frac{\rho^2 I^*_{zz}}{\varkappa G}\frac{\partial^4 w}{\partial t^4}+\frac{EI^*_{zz}}{\varkappa AG}\frac{\partial^2 f}{\partial x^2}-\frac{\rho I^*_{zz}}{\varkappa AG}\frac{\partial^2 f}{\partial t^2}=f(x,t) \quad (20)$$

In the same manner, the forced edge-wise vibration of a nonuniform Timoshenko beam is obtained as:

$$\frac{\partial^2}{\partial x^2}\left(EI^*_{yy}(x)\frac{\partial^2 v(x,t)}{\partial x^2}\right)+\rho A(x)\frac{\partial^2 v(x,t)}{\partial t^2} -\frac{\partial}{\partial x}\left(\rho I^*_{yy}(x)\left(1+\frac{E}{\varkappa G}\right)\frac{\partial^3 v}{\partial x\partial t^2}\right) +\frac{\rho^2 I^*_{yy}}{\varkappa G}\frac{\partial^4 v}{\partial t^4}+\frac{EI^*_{yy}}{\varkappa AG}\frac{\partial^2 f}{\partial x^2}-\frac{\rho I^*_{yy}}{\varkappa AG}\frac{\partial^2 f}{\partial t^2}=f(x,t) \quad (21)$$

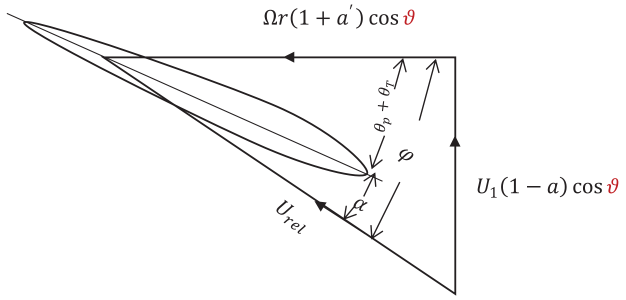

Fig. 7. Blade element velocities.

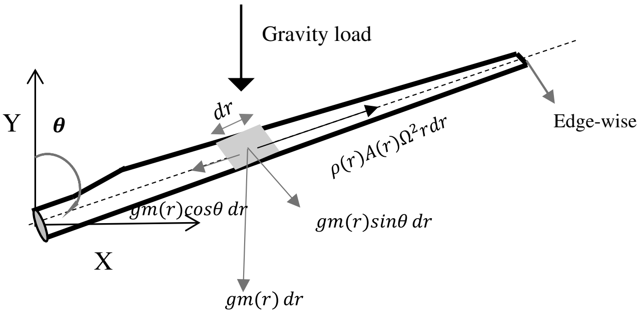

Fig. 8. Gravitational load components acting on the blade in the edge-wise direction.

where G denotes the modulus of rigidity of the material and $\varkappa$ is a consnt, known as Timoshenko's shear coefficient, which depends on the shape of the cross-section. Plots for mass per unit length and stiffness along the blade span, according to the data in [12], are presen[ted] in Figs. 3 and 4, respectively, to help clarify the complicated distribution of blade mass and stiffness along the blade span. In this study, the correction shear factor starts at the value of 0.9 as the first section has a circular cross-section and decreases with distance along the blade according to the chord and thickness of different blade aerofoils [12].

C. AERODYNAMIC MODULE

Blade element momentum theory is used to calculate the aerodynamic loads. This theory is based on integrating the 2D aerofoil aerodynamic loading along the blade span. In this theory, the force of a blade element is solely responsible for the change of momentum of the air that passes through the annulus swept by the element. The deformation in the flap-wise and edge-wise directions is shown in Fig. 5. The flow through each blade section at radius r is assumed to be a two-dimensional flow, as shown in Fig. 6. According to [25], the components of aerodynamic forces on a blade element are

Table I. MW NREL blade sections and aerofoils [12]

Section	Position (m)	Chord (m)	Twist (°)	Aerofoil
1	2.87	3.542	13.308	Cylinder 1
2	5.60	3.854	13.308	Cylinder 1
3	8.33	4.167	13.308	Cylinder 2
4	11.75	4.557	13.308	DU40_A17
5	15.85	4.652	11.480	DU35_A17
6	19.95	4.458	10.162	DU35_A17
7	24.05	4.249	9.011	DU30_A17
8	28.15	4.007	7.795	DU25_A17
9	32.25	3.748	6.544	DU21_A17
10	36.35	3.502	5.361	DU21_A17
11	40.45	3.256	4.188	NACA_64_618
12	44.55	3.01	3.125	NACA_64_618
13	48.65	2.764	2.319	NACA_64_618
14	52.75	2.518	1.526	NACA_64_618
15	56.17	2.313	0.863	NACA_64_618
16	58.90	2.086	0.370	NACA_64_618
17	61.63	1.419	0.106	NACA_64_618

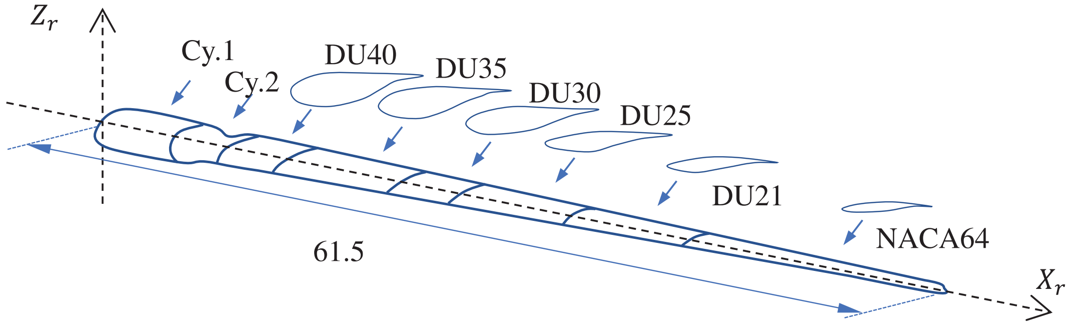

Fig. 9. Schematic of the NREL blade. [12].

$$\overrightarrow{f_{aero}} = \overrightarrow{i_{YZ}}\begin{Bmatrix} \mathfrak{f}_T \\ \mathfrak{f}_N \end{Bmatrix} = \overrightarrow{i_{YZ}}\begin{Bmatrix} (\mathscr{L}\sin(\alpha+\beta) - \mathcal{D}\cos(\alpha+\beta))\cos\vartheta \\ (\mathscr{L}\cos(\alpha+\beta) + \mathcal{D}\sin(\alpha+\beta))\cos\vartheta \end{Bmatrix} \quad (22)$$

with

$$\mathcal{L} = o.5\rho_a c C_l {U_{rel}}^2 \quad (23)$$

$$\mathcal{D} = o.5\rho_a c C_d {U_{rel}}^2 \quad (24)$$

where $\mathfrak{f}_T,\mathfrak{f}_N$ are the aerodynamic forces in the directions of $\overrightarrow{l_{YZ}}$, $\mathfrak{f}_T$ in the tangential to the circle swept by the rotor, and $\mathfrak{f}_N$ is normal to the plane of rotation along the blade's different sections [27], $\mathcal{L},\mathcal{D}$ are the lift and drag for[ces]for unit blade length, C_l,C_d are the lift and drag coefficients, ρ_a,c are air density and chord length, and α is the angle of attack. The total pitch angle β is the sum of the element twist angle and the blade pitch angle at the blade section under consideration.

$$U_{rel} = \sqrt{[U_a(1-a)\cos\vartheta]^2 + [r\Omega(1+a')\cos\vartheta]^2} \quad (25)$$

$$\alpha = \arctan\left(\frac{U_a(1-a)}{r\Omega(1+a')}\right) - (\beta) \quad (26)$$

where U_a is the airflow velocity, r,Ω are the rotation radius of the blade element and angular velocity, ϑ,β are, respectively, the angle of precone and the total pitch angle of the blade element, $a,a^{'}$ are the induction velocity factors and solved by iteration, as shown in Fig. 7.

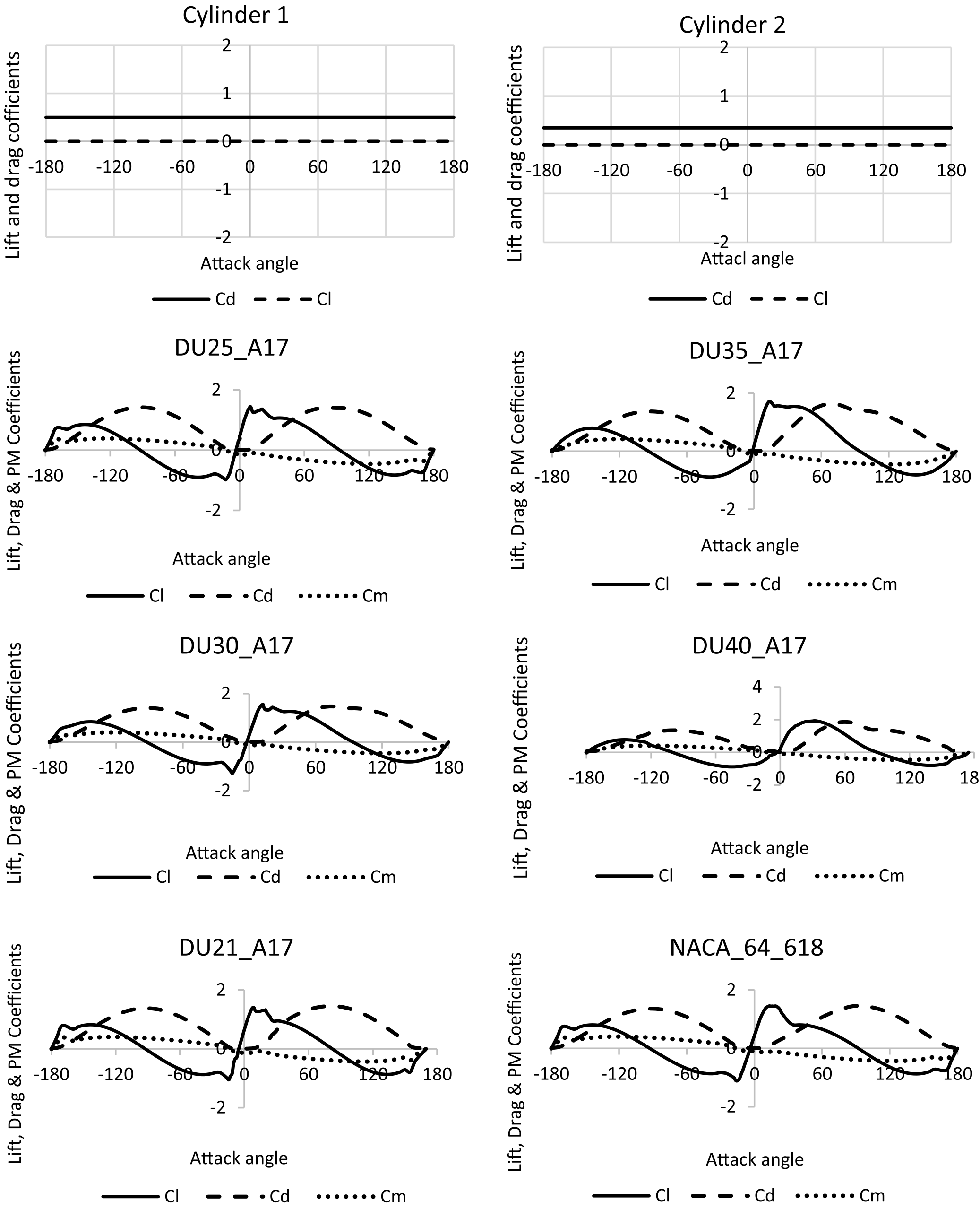

Fig. 10. Aerodynamic coefficient of the aerofoils in the 5 MW NREL wind turbine blade [12].

The axial and angular induction factors are as follows [25]:

$$\frac{a}{1-a}=\frac{\sigma_r}{4sin\varphi}\left[\left(C_l\cos\varphi+C_d\sin\varphi\right)-\frac{\sigma_r}{4sin^2\varphi}\left(C_l\sin\varphi-C_d\cos\varphi\right)^2\right] \tag{27}$$

$$\frac{a}{1+a'}=\frac{\sigma_r\left(C_l\sin\varphi-C_d\cos\varphi\right)}{4\sin\varphi\cos\varphi} \tag{28}$$

where chord solidity, σ_r, is defined as the blade chord at a certain blade element divided by the circumferential length at that position $\sigma_r=\frac{Bc}{2\pi rcos\vartheta}$. The angle φ is the angle between the plane of rotation and the relative velocity.

The dynamic response of the HAWT blade to the fluctuating aerodynamic loads is investigated by means of modal analysis [25], in which the excitations of the various different natural modes of vibration are computed separately, and the results are superposed as:

$$w(X_r,t)=\sum_{j=1}^{n}\delta_j(t)u_j(x) \tag{29}$$

$$v(X_r,t)=\sum_{j=1}^{n}q_j(t)U_j(x) \tag{30}$$

where $u_j(x)$ and $U_j(x)$ are the j^{th} mode shape in the flap-wise and edge-wise directions, respectively, arbitrarily assumed

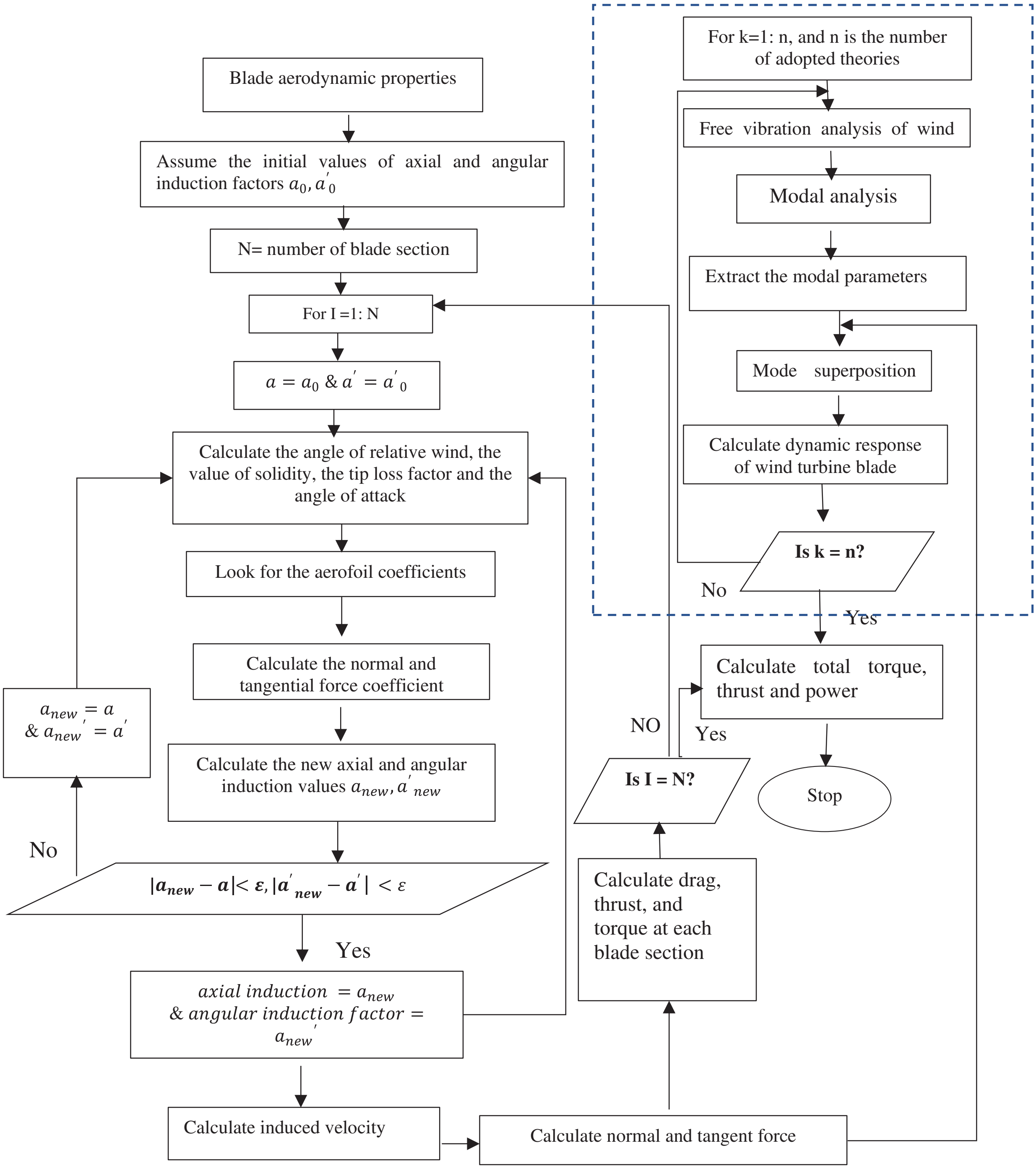

Fig. 11. Forced vibration computational procedure.

to have a value of unity at the blade tip, and $\delta_j(t)$ and $q_j(t)$ are the variation of displacement in both directions.

D. GRAVITATIONAL LOAD

The purpose of this section is to propose an expression for the edge-wise dynamic effect of gravitational force on the HAWT blade. Variation in the azimuth angle θ means that the gravitational force introduces an oscillating stiffness that changes with azimuth angle, with a consequent large dynamic response in the edge-wise direction. The blade is assumed to start its motion from the vertical position, where the azimuth angle is equal to 0. Maximum effect of gravitational load occurs at the horizontal position of blade at azimuth angle 90° which is assumed to be the position of maximum dynamic deflection. Figure 8 shows the direction of the gravitational load, and direction and its component acting on the blade in the edge-wise direction.

III. RESULTS AND DISCUSSION

As with any dynamic system, the response of a forced wind turbine blade depends primarily upon the blade's dynamic characteristics such as natural frequencies, its damping, mode shapes, and the characteristics of the excitation force to which it is subjected [25]. The 5 MW blade used in this study is a three-bladed HAWT, developed by NREL as shown in Fig. 9.

The rated output power of the blade is 5 MW, and the rotational speed = 12.1 rpm in a wind speed = 11.4 m/s. The aerodynamic properties such as chord length, twist angle, the position of each section along the blade span, and aerofoil type are listed in Table I [12].

The specifications of the 5 MW NREL are introduced as input parameters. Each wind turbine blade is divided into 17 elements, and each part coincides with a particular aerofoil shape. Figure 10 shows the aerodynamic

Table II. Natural frequencies for the first 10 modes at angular speed $\Omega = 0$ rpm in the flap-wise direction for Rayleigh beam, rotating Bernoulli beam, nonrotating Bernoulli beam, and Rayleigh beam with pitch and precone angles effects and results for NREL 5 MW HAWT blade [15,16,21]

	Method									
Mode no.	Rayleigh with blade parameters: present work	Rayleigh (Hz) present: work	B-Modes (Hz) [NREL]	FAST (Hz) [NREL]	Jeong *et al.*, (20) (Hz)	Li *et al.*, [16] (Hz)	Jokar *et al.*, [15] (Hz)	Bernoulli present work	Rot Bernoulli: present work	Timoshenko: present work
1	0.680	0.680	0.69	0.68	0.673	0.68	0.727	0.681	0.681	0.678
2	1.985	1.985	2.00	1.94	1.926	1.98		3.060	3.059	1.960
3	4.543	4.543	4.69	4.43	4.427	4.66		3.915	3.914	4.427
4	8.132	8.132						8.168	8.167	7.808
5	12.674	12.674						12.763	12.762	11.980
6	18.031	18.031						18.210	18.209	16.774
7	24.214	24.214						24.529	24.528	22.185
8	31.323	31.323						31.856	31.855	28.199
9	39.565	39.565						40.160	40.159	36.876
10	48.194	48.194						49.974	49.973	40.022

Timo. = Timoshenko, Bern. = Bernoulli.

Table III. Natural frequency comparisons for the different beam theories and results for NREL 5 MW HAWT blade [15,16,21] in the flap-wise and edge-wise directions of a single blade without an aerodynamic force

No.	Rayleigh (Hz) present	B Modes Hz [NREL]	FAST Hz [NREL]	[16] (Hz)	[21] (Hz)	Rayleigh +angles (Hz) present	Rot Bern. (Hz) present	Timo. (Hz) present	Bern. (Hz) present
1	0.68 F	0.69 F	0.68 F	0.67 F	0.68 F	0.68 F	0.68 F	0.67 F	0.68
		−1.459%	0%	1.481%	0%	0%	0%	1.481%	0%
2	1.11 E	1.12 E	1.10 E	1.11 E	1.10 E	1.11 E	1.11 E	1.09 E	1.11 E
		−0.896%	0.904%	0%	0.904%	0%	0%	1.818%	0%
3	1.98 F	2.00 F	1.94 F	1.92 F	1.98 F	1.98 F	3.05 F	1.95 F	3.05 F
		−1.005%	2.040%	3.076%	0%	0%	−42.54%	1.526%	−42.54%
4	4.10 E	4.12 E	4.00 E	3.96 E	3.99 E	4.18 E	3.91 F	3.98 E	3.91 F
		−0.486%	2.469%	3.473%	2.719%	0%	4.744%	2.970%	4.744%
5	4.54 F	4.69 F	4.43 F	4.43 F	4.66 F	4.54 F	4.20 E	4.42 F	4.21 E
		−3.250%	2.452%	2.452%	−2.608%	0%	7.780%	2.678%	7.542%

F = Flap, E = Edge, Timo. = Timoshenko, Bern. = Bernoulli.

coefficients of different aerofoils versus the angle of attack. The flowchart of the forced vibration computational procedure is shown in Fig. 11. At each blade section, the angle of relative speed and the angle of attack are calculated. Free vibration analysis is formulated for each adopted theory to extract the modal parameters. Aerodynamic loads are determined at each element and applied as external distributed forces for each model.

Table II shows the natural frequencies in the flap-wise direction obtained by applying the different beam theories, that is, (1) Rayleigh, (2) Rayleigh with the effect of control angles, (3) Timoshenko, (4) rotating Bernoulli, and (5) non-rotating Bernoulli beams, using the same geometry and material properties as the NREL 5 MW HAWT blade as [12]. The comparison is made against the B-modes, FAST codes, and results from [16,21]. It was found that the results obtained by the present study agree well with the numerical and experimental results from other investigations. The fundamental frequencies obtained in this study have approximately the same values, which indicates that

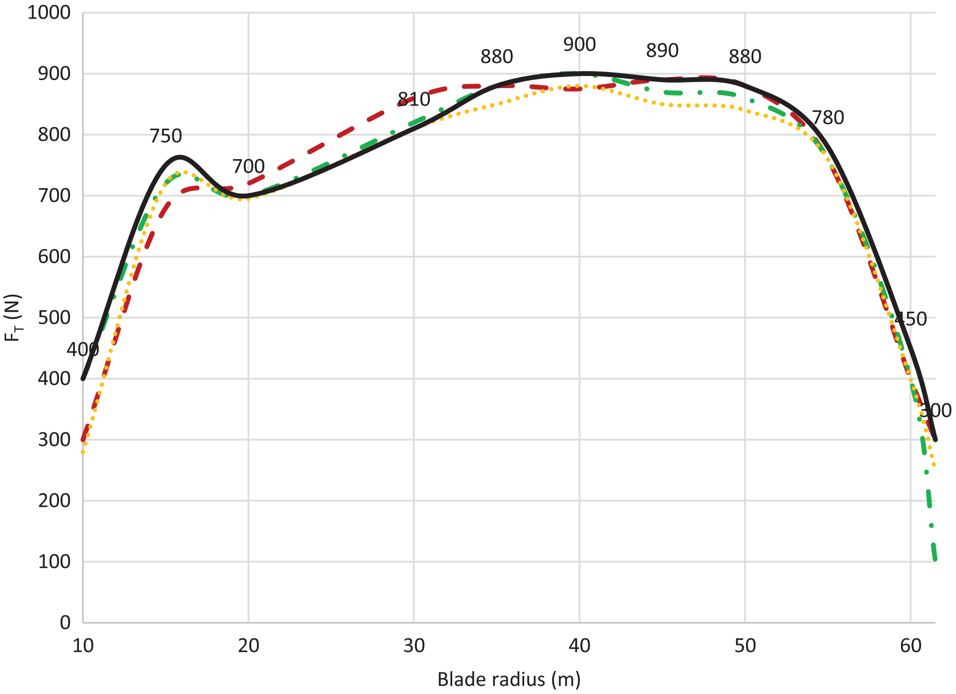

Fig. 12. The tangential force due to the aerodynamic load distribution along blade span at the rated operating condition; the black solid curve is the results of the present work, while the yellow dotted line represents the data adopted from [16], the green dash-dotted line represents the data from [21], and the red dashed line represents the data from [23].

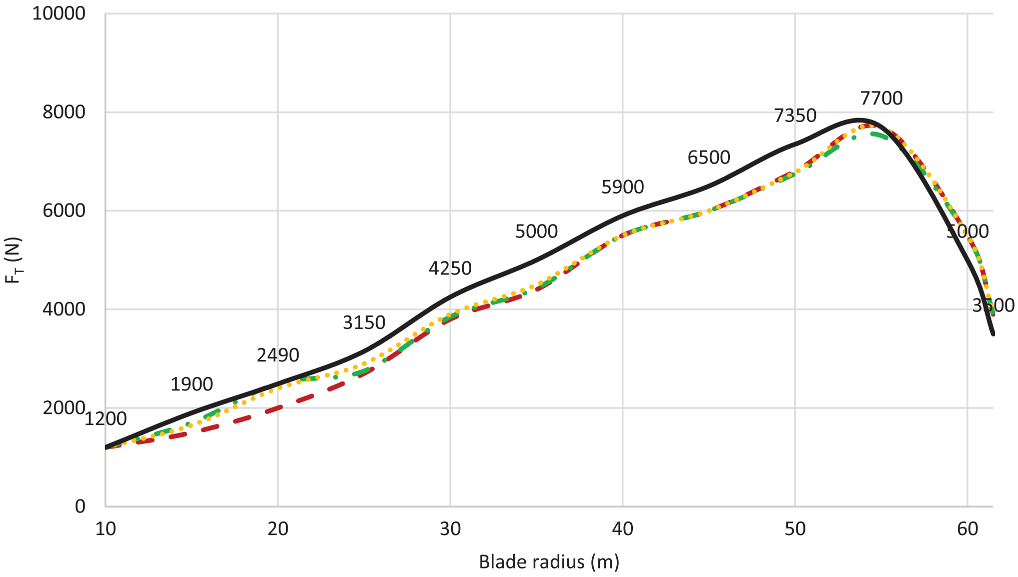

Fig. 13. The normal force due to the load distribution along the blade span at the rated operating condition; the black solid curve is the results of the present work, while the yellow dotted line represents the data adopted from [16], the green dash-dotted line represents the data from [21], and the red dashed line represents the data from [23].

ignoring the influence of centrifugal force when the blade is stationary leads to the same results for the fundamental mode. There are differences in the second frequency obtained using the Bernoulli and rotating Bernoulli theories from the others. From Table II, the second natural frequency obtained by Bernoulli and rotating Bernoulli theories increased by 42.8% compared to its counterpart determined by Rayleigh theory. This will be checked as it affects the dynamic response. Table III shows the first five natural frequencies in the flap-wise and edge-wise directions. It can be seen that the values of the third and fourth frequencies of Bernoulli and rotating-Bernoulli (which represent the third and fourth flap-wise frequencies) are close to each other but do not agree with the same modal values as obtained using the other theories.

From the theories being considered, the Rayleigh model is chosen as the most comprehensive model to compare with other investigations. The comparison will, firstly, compare the aerodynamic loading with results reported in the literature that adopted different aerodynamic methods. Then, the dynamic response in the flap-wise and edge-wise directions is compared with other studies reported in the literature that adopted different structural analyses. The aerodynamic load distribution along the blade span at the rated operating condition in the normal and tangent direction is illustrated in Figs. 12 and 13, which show the results of this study generally agree well with data reported in the literature despite small discrepancies in some blade sections.

The distribution of dynamic displacement response in the edge-wise direction along the blade span is shown in Fig. 14. The figure shows a comparison between the results obtained by the present study and those obtained using commercial software such as BEM-ABAQUS [21], CFD-computational structural dynamics (CSD) models [23] model, and results reported in [16]. The deflection in the flap-wise direction along the blade span due to the aerodynamic loading is shown in Fig. 15. For comparison, the figure also shows results reported in [16,21,23]. All the compared studies show some dynamic response discrepancies at some positions along the blade span.

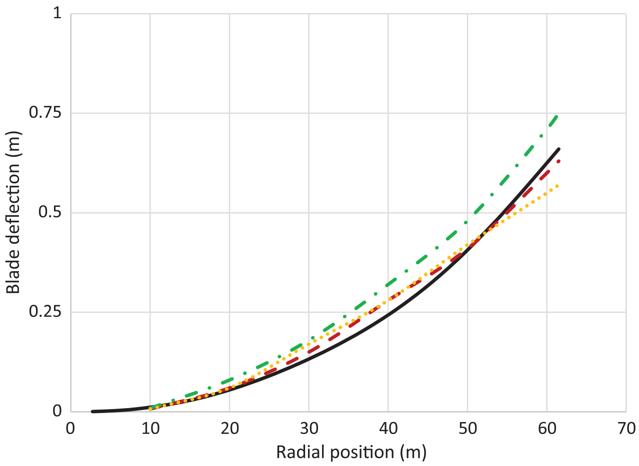

Fig. 14. Blade deflection in the edge-wise direction due to the aerodynamic loading and gravitational force; the black solid curve is the results of the present work compared with the yellow dotted line (data are adopted from [16]), the green-dotted line (data are adopted from [21] where BEM-ABAQUS was applied), and the red dashed line (data are adopted from [23] where CFD-CSD was applied).

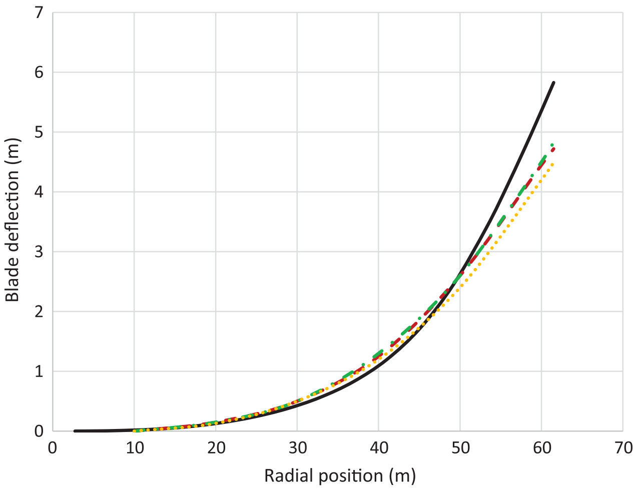

Fig. 15. Blade deflection in the flap-wise direction due to the aerodynamic loading; the black solid curve is the results of the present work compared with the yellow dotted line (data are adopted from [16]), the green-dotted line (data are adopted from [21] where BEM-ABAQUS was applied), and the red dashed line (data are adopted from [23] where CFD-CSD was applied).

Table IV shows additional results from previous publications regarding tip blade deflection due to the flap-wise (out-of-plane) and edge-wise (in-plane) vibrations, thrust force, and rotor power. Table IV, row 1, represents the results obtained by Li Z *et al.*, [16], where a geometrically exact beam model and BEM theory were used to obtain the blade deformation in both directions of the 5 MW NREL blade. Similarly, row 2 represents the results of Sabale and Gopal [19], where BEM-EBM were used for the same blade, while row 3 represents the results obtained from [12] where the B-Mods FAST software developed by NREL was used. Row 4 represents the data obtained from reference [23] using a CFD flow solver and blade elastic deformation; row 5 represents the results obtained from Ponta *et al.*, [14], where the generalized Timoshenko beam theory was adopted to model the 5 MW NREL blade. Row 6 represents the results of Sabale and Gopal [20], where BEM-EBM were used to model the 5 MW NREL blade, while row 7 presents the results from [21] calculated using the commercial software ABAQUS for the same NREL blade. Bernoulli beam theory was adopted to the same proposed blade to obtain the results in [18], row 8.

The results presented in rows 9–13 were obtained in this study by applying the Rayleigh, Rayleigh with added blade angles, Timoshenko beam, rotating Bernoulli, and nonrotating Bernoulli theories, respectively. The previous results between rows 1–8 in Table IV are compared with those obtained in the present study using the different beam models with BEM theory to calculate the aerodynamic loads. It was found that the results obtained from the present study agree with [12], where B-Mods and FAST software were used. The flap-wise tip deflection agrees with [21], where the elastic deformation of the blade was calculated using the FE commercial software ABAQUS, although the edge-wise deflection was significantly larger. The method adopted in [16,19,21] for the structural analysis was the

Table IV. Comparison of the dynamic response under nominal working conditions of the present study and references [12,14,16,18–21] where the same model of 5 MW NREL wind turbine blade was adopted

No.	Reference	Flap-wise deflection m	Edge-wise deflection m	Rotor power MW	Thrust force KN
1	Li Z *et al.*, 2020 [16]	4.49	−0.57	5.3	678.44
2	Sabal & Gopal, 2019a [19]	4.41	−0.57	4.97	690.72
3	Jonkman *et al.*, 2009 [12]	5.47	−0.61	5.28	814.45
4	Yu & Kwon, 2014 [23]	4.72	−0.63	5.22	656.43
5	Ponta *et al.*, 2016 [14]	3.85	−0.56	5.19	660.19
6	Sabale & Gopal, 2019b [20]	4.55	−0.62	5.17	676.12
7	Jeong *et al.*, 2014 [21]	4.83	−0.75	–	–
8	Rezaei *et al.*, 2016 [18]	8.35	−1.85	–	–
9	Rayleigh theory (present work)	5.827	−0.660	5.38	687
10	Rayleigh+ angles effect (present)	5.827	−0.660	5.38	687
11	Timoshenko theory (present)	5.500	−0.659	5.38	687
12	Rotating Bernoulli (present)	5.378	−0.658	5.38	687
13	Nonrotating Bernoulli (present)	5.341	−0.658	5.38	687

geometrically exact beam theory, and some differences can be noticed in the results. [14] adopted the Timoshenko beam theory for free vibrations, but it can be seen that the flap-wise deformation is small compared with other results. On the other hand, the results in [18] obtained from applying the Bernoulli theory for structural analysis of the blade showed relatively large deflection values in both directions. The results in rows 9 and 10 are the same, which indicates that the pitch and precone angles may not affect the dynamic response. The same conclusion can be seen in Table II, where the natural frequencies in columns 1 and 6 have the same values. The comparison with previously published results of the dynamic responses under nominal working conditions, thrust force, and rotor power shown in Table IV has a range of output results due to the different structural parameters adopted, with the present results that are very much on a par with each other for flap-wise and edge-wise deflections.

The spanwise distributions of blade deflection under the operational aerodynamic force in the flap-wise direction are shown in Fig. 16. The dynamic deflections predicted by all the theories considered are represented in the figure. The discrepancies between Bernoulli and rotating Bernoulli and the other theories due to the flap-wise vibration can be seen. Despite the difference that can be seen in Table IV and also reported in [14,18], Ponta *et al.*, [14] adopted the Timoshenko beam theory for free vibration analysis, and the blade tip deflection in the flap-wise direction (3.85 m) is the smallest of the predicted values shown in Table IV. Rezaei *et al.*, [18] adopted the Bernoulli theory for free vibration analysis, and it can be seen that the blade tip deflection is the largest in both the flap-wise and edge-wise directions (8.35 m and 1.85 m, respectively). The studies reported here adopted different codes such as ABAQUS, FAST, B-Mods, and ANSYS commercial finite element software to find the modal dynamic characteristics of the given blade. While all the results in this study were found using the same code and numerical techniques, the difference that appears in the frequencies values as shown in Tables II and III and the deflection values as shown in Table IV are due to the discrepancies in the numerical methods that used in each code.

Figure 16 illustrates the flap-wise deflection along the blade span agreed well for the Rayleigh model, Rayleigh model with control angle, and Timoshenko model, though the Timoshenko model results do show some small discrepancies. This result also appears in mode two for flap-wise natural frequencies, as shown in Tables II and III. At the same time, the flap-wise result, obtained by applying Bernoulli and rotating Bernoulli approaches, shows less accurate results in the end quarter of the blade. The absence of the rotary inertia effect could be the reason for this.

The dynamic deflection due to the edge-wise vibration is shown in Fig 17 for all the theories considered in this study. Unlike the results obtained for the flap-wise deflections, the dynamic deflection in the edge-wise direction has similar results along the blade span for all the theories considered. This could be because the blade's stiffness in the edge-wise direction is larger than the stiffness in the flap-wise direction.

Figure 18 presents the predicted flap-wise slope dynamic response along the blade span for all the theories

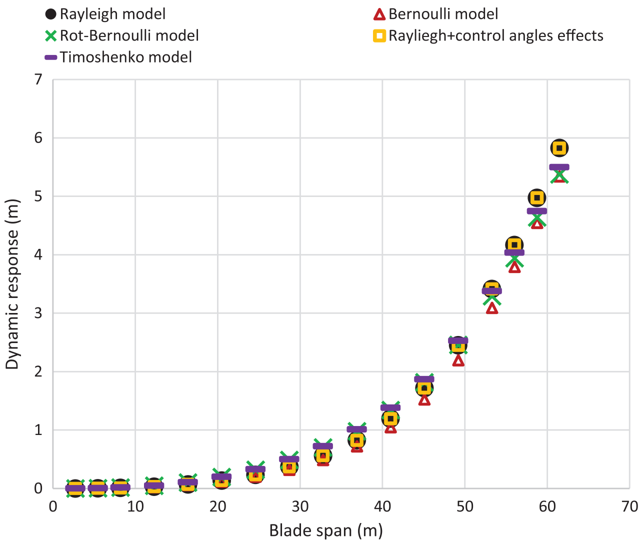

Fig. 16. Flap-wise deflection distribution along the blade span as predicted by the theories considered in this paper.

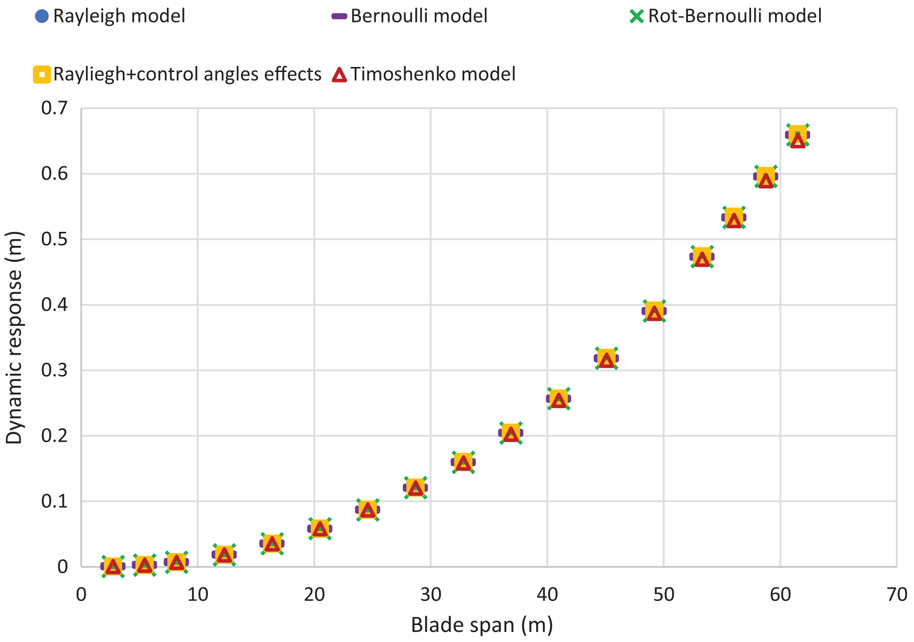

Fig. 17. Edge-wise deflection distribution along the blade span.

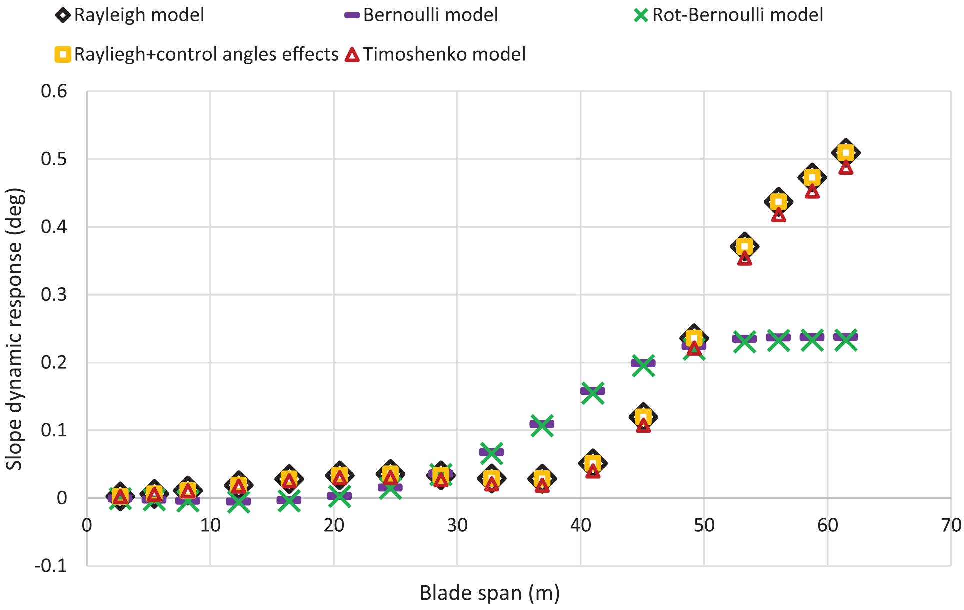

Fig. 18. Flap-wise slope distribution along the blade span.

considered in this study, and significant discrepancies can be noticed. We see the Bernoulli and rotating Bernoulli theories produce much the same results, but these diverge substantially from the results produced by the other theories considered, which have much the same distribution. Figure 18 shows that the slope values in the length from 30 m to 45 m from the blade root obtained using Bernoulli and rotating Bernoulli are much greater than those obtained using Rayleigh and Timoshenko based models, while the slope values in the end blade quarter are much greater using Rayleigh and Timoshenko theories.

The discrepancies in slope begin in the first quarter of the blade length, whereas when considering the transverse deflection in Fig. 16, the differences did not appear until the last quarter of the blade span. This result may indicate that slope deflection is a more accurate comparison method.

The structural behavior of a wind turbine blade will depend on the blade's parameters used in the analysis. The blade deformation is predominantly due to different, complex aerodynamic loads. Each rotor revolution causes a complete gravity stress reversal in the low-speed shaft. In addition, the deformation stresses are due to the out-of-plane loading cycle arising from the combined wind load. In this study, the dynamic response is determined based on the modal characteristics of the theory being considered and the relative discrepancies in the dynamic response between the theories observed. Figure 19 demonstrates the slope angle distribution due to edge-wise vibration. All the adopted

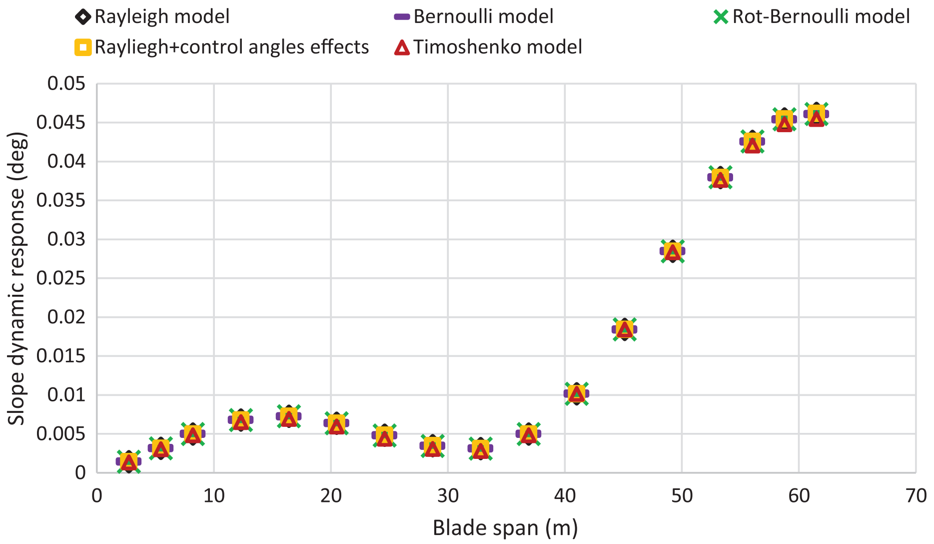

Fig. 19. Edge-wise slope distribution along the blade span.

theories demonstrate the same slope values along the blade span, indicating that the blade's stiffness in the edge-wise direction is larger than the flap-wise direction. Figures 17 and 19 demonstrate the similarities in the deflection values of the theories considered.

IV. CONCLUSION

This paper investigated the effects of deformation parameters on the dynamic characteristics of the NREL 5 MW offshore wind turbine blade using different beam theories. The dynamic response was calculated based on the model features of each theory to observe the discrepancies between the different theories in terms of the net energy, considered as the sum of the products of forces as expressed in the governing equations 11–21. The main conclusions of the study are summarized as follows:

A comparison of simulated natural frequencies indicates that the free vibration analysis in the flap-wise direction is approximately the same for the Rayleigh and Rayleigh with adding the blade control angles such as the pitch precone angles. An important conclusion is that Bernoulli and rotating Bernoulli's theories produce different natural frequencies values at second and third mode, while the Rayleigh model produces lower frequencies values at higher modes than the Bernoulli and rotating Bernoulli's models in the flap-wise direction.

There are similarities in the flap-wise dynamic response between Bernoulli and rotating Bernoulli but substantial differences in the slope compared to the other models considered. These differences in the slope may indicate the importance of the rotary inertia effect, which is not included in the Bernoulli and rotating Bernoulli models.

The difference between theories in the edge-wise deflection is not as apparent as the flap-wise deflection. It may be because the force acting along the edge-wise direction is significantly less than the one along the flap-wise direction. In addition, the stiffness in the edge-wise tends to be higher.

The dynamic slope distribution along the blade span indicates differences between the theories considered due to differences in the flap-wise vibration. In contrast, the dynamic slope distribution for the edge-wise slope showed a close agreement of all theories considered due to agreement on the edge-wise vibration.

CONFLICT OF INTEREST STATEMENT

The authors declare no conflicts of interest.

References

[1] D. Gielen, R. Gorini, N. Wagner, R. Leme, L. Gutierrez, G. Prakash, E. Asmelash, L. Janeiro, G. Gallina, G. Vale, and L. Sani, *Global Energy Transformation: A Roadmap to 2050*: International Renewable Energy Agency (IRENA), Apr. 2019.

[2] W. Stoddard, "The life and work of Bill Heronemus, wind engineering pioneer," *Wind Eng.*, vol. 26, no. 5, pp. 335–341, Sep. 2002.

[3] Gemma N Thomas, *Wind Energy in the UK: June 2021*: Office for National Statistics. Available: https://www.ons.gov.uk/economy/environmentalaccounts/articles/windenergyintheuk/june2021#wind-electricity-generation-in-the-uk. June 2021.

[4] M. A. Shohag, E. C. Hammel, D. O. Olawale, and O. I. Okoli, "Damage mitigation techniques in wind turbine blades: a review," *Wind Eng.*, vol. 41, no. 3, pp. 185–210, Jun. 2017.

[5] J. Moccia, J. Wilkes, I. Pineda, and G. Corbetta, *Wind Energy Scenarios for 2020*: European Wind Energy Association Report, EWEA, p. 3. Available: http://www.ewea.org/fileadmin/files/library/publications/reports/EWEA-Wind-energy-scenarios-2020.pdf. Jul. 2014.

[6] S. Campbell, "Annual blade failures estimated at around 3800," *Wind Power Monthly*, p. 14. Available: https://www.windpowermonthly.com/article/1347145/annual-blade-failures-estimated-around-3800. May 14, 2015.

[7] A. Robertson, J. Jonkman, F. Vorpahl, W. Popko, J. Qvist, L. Frøyd, X. Chen, J. Azcona, E. Uzunoglu, C. Guedes Soares, and C. Luan, "Offshore code comparison collaboration continuation within IEA wind task 30: phase II results regarding a floating semisubmersible wind system," in *Int. Conf. Offshore Mech. Arctic Eng.*, American Society of Mechanical Engineers, vol. 45547, p. V09BT09A012, Jun. 8, 2014.

[8] R. Rafiee, M. Tahani, and M. Moradi, "Simulation of aeroelastic behavior in a composite wind turbine blade," *J. Wind Eng. Ind. Aerodyn.*, vol. 151, pp. 60–69, Apr. 1, 2016.

[9] W. Hu, K. K. Choi, O. Zhupanska, and J. H. Buchholz, "Integrating variable wind load, aerodynamic, and structural analyses towards accurate fatigue life prediction in composite wind turbine blades," *Struct. Multidiscip. Optim.*, vol. 53, no. 3, pp. 375–394, Mar. 2016.

[10] Y. Li, A. M. Castro, T. Sinokrot, W. Prescott, and P. M. Carrica, "Coupled multi-body dynamics and CFD for wind turbine simulation including explicit wind turbulence," *Renew. Energy*, vol. 76, pp. 338–361, Apr. 1, 2015.

[11] W. Mo, D. Li, X. Wang, and C. Zhong, "Aeroelastic coupling analysis of the flexible blade of a wind turbine," *Energy*, vol. 89, pp. 1001–1009, Sep. 1, 2015.

[12] J. Jonkman, S. Butterfield, W. Musial, and G. Scott, *Definition of a 5-MW Reference Wind Turbine for Offshore System Development*. Golden, CO, USA: National Renewable Energy Lab. (NREL), Feb. 1, 2009.

[13] J. Rosen, I. Tietze-Stöckinger, and O. Rentz, "Model-based analysis of effects from large-scale wind power production," *Energy*, vol. 32, no. 4, pp. 575–583, Apr. 1, 2007.

[14] F. L. Ponta, A. D. Otero, L. I. Lago, and A. Rajan, "Effects of rotor deformation in wind-turbine performance: the dynamic rotor deformation blade element momentum model (DRD–BEM)," *Renew. Energy*, vol. 92, pp. 157–170, Jul. 1, 2016.

[15] H. Jokar, M. Mahzoon, and R. Vatankhah, "Dynamic modeling and free vibration analysis of horizontal axis wind turbine blades in the flap-wise direction," *Renew. Energy*, vol. 146, pp. 1818–1832, Feb. 1, 2020.

[16] Z. Li, B. Wen, X. Dong, Z. Peng, Y. Qu, and W. Zhang, "Aerodynamic and aeroelastic characteristics of flexible wind turbine blades under periodic unsteady inflows," *J. Wind Eng. Ind. Aerodyn.*, vol. 197, p. 104057, Feb. 1, 2020.

[17] A. Algolfat, W. Wang, and A. Albarbar, "Comparison of beam theories for characterisation of a NREL wind turbine blade flap-wise vibration," *Proc. Inst. Mech. Eng., Part A: J. Power Energy*, vol. 236, p. 09576509221089146, Apr. 28, 2022.

[18] M. M. Rezaei, M. Behzad, H. Moradi, and H. Haddadpour, "Modal-based damage identification for the nonlinear model of modern wind turbine blade," *Renew. Energy*, vol. 94, pp. 391–409, Aug. 1, 2016.

[19] A. Algolfat, W. Wang, and A. Albarbar, "Study of centrifugal stiffening on the free vibrations and dynamic response of offshore wind turbine blades," *Energies*, vol. 15, no. 17, p. 6120, Jan. 2022.

[20] A. K. Sabale and N. K. Gopal, "Nonlinear aeroelastic analysis of large wind turbines under turbulent wind conditions," *AIAA J.*, vol. 57, no. 10, 4416–4432, Oct. 2019.

[21] M. S. Jeong, M. C. Cha, S. W. Kim, I. Lee, and T. Kim, "Effects of torsional degree of freedom, geometric nonlinearity, and gravity on aeroelastic behavior of large-scale horizontal axis wind turbine blades under varying wind speed conditions," *J. Renew. Sustain. Energy*, vol. 6, no. 2, p. 023126, Mar. 25, 2014.

[22] M. Sayed, L. Klein, T. Lutz, and E. Krämer, "The impact of the aerodynamic model fidelity on the aeroelastic response of a multi-megawatt wind turbine," *Renew. Energy*, vol. 140, pp. 304–318, Sep. 1, 2019.

[23] D. O. Yu and O. J. Kwon, "Predicting wind turbine blade loads and aeroelastic response using a coupled CFD–CSD method," *Renew. Energy*, vol. 70, pp. 184–196, Oct. 1, 2014.

[24] A. Sabale and K. N. Gopal, "Nonlinear aeroelastic response of wind turbines using Simo-Vu-Quoc rods," *Appl. Math. Model.*, vol. 65, 696–716, Jan 1. 2019.

[25] T. Burton, N. Jenkins, D. Sharpe, and E. Bossanyi, *Wind Energy Handbook*: John Wiley & Sons, Chichester, New York, Weinheim, Brisbane, Singapore, Toronto May 18, 2011.

[26] S. S. Rao, *Mechanical vibrations laboratory manual*: Edition Addison-Wesley Publishing Company, [Sl] 1995.

[27] J. F. Manwell, J. G. McGowan, and A. L. Rogers, *Wind Energy Explained: Theory, Design and Application*: John Wiley & Sons, University of Massachusetts, Amherst, USA. Sep. 14, 2010.